Available online at www.sciencedirect.com
ScienceDirect
International Journal of Heat and Mass Transfer 50 (2007) 3749–3766
International Journal of HEAT and MASS TRANSFER
www.elsevier.com/locate/ijhmt

Analysis of different RANS models applied to turbulent forced convection

J.E. Jaramillo, C.D. Pérez-Segarra, A. Oliva *, K. Claramunt

Centre Tecnològic de Transferència de Calor, Lab. Termotècnia i Energètica, Universitat Politècnica de Catalunya (UPC), ETSEIAT, C/Colom 11, 08222 Terrassa, Spain

Received 13 April 2006
Available online 16 April 2007

Abstract

The aim of this work is to study the adequacy of different RANS models in terms of accuracy and numerical performance in the description of turbulent internal forced convection flows. Within RANS modelizations, linear and non-linear eddy-viscosity models and explicit algebraic models are explored. A comparison of the suitability of different two-equation platforms such as k–ϵ and k–ω is also carried out. Three different internal forced convection flows are studied: turbulent plane channel, backward facing step, and confined impinging slot jet. The results are compared with DNS or experimental data available in the literature, reviewing mean and fluctuating velocities, turbulent stresses and global parameters like Nusselt number, skin friction coefficient or reattachment point. Governing partial differential equations are transformed to algebraic ones by a general fully implicit finite-volume method over structured and staggered grids. A segregated SIMPLE-like algorithm is used to solve pressure-velocity fields coupling. A verification procedure based on the generalised Richardson extrapolation is applied to ensure the credibility of the numerical solutions.

Keywords: RANS; Two-equation; Non-linear; Channel flow; Backward facing step; Impinging slot jet

1. Introduction

Turbulence plays an important role in engineering applications as most flows in industrial equipment and surroundings are in turbulent regime. Direct Numerical Simulation (DNS) of these flows using full 3D and time dependent Navier–Stokes (NS) equations is generally restricted to simple geometries and low Reynolds number flows due to the large, if not prohibitive, computational resources required to resolve all the scales of motion. Therefore, the use of turbulence modelling employing statistical techniques for high Reynolds numbers or complex geometries is still necessary. In general, this modelization can be based on volume filtering (Large Eddy Simulation, LES) or time averaging (Reynolds-Averaged Navier–Stokes Simulations, RANS) of the NS-equations. LES models are still too expensive for routine calculation because, even though the smallest eddies are modelled, the larger ones have to be solved in detail (3D and unsteady). Otherwise, RANS models can be appropriate to describe most of the main characteristics of the fluid motions [1].

In the past decades RANS-technique has received great interest because of its wide range of applicability and reasonable computational cost. This technique solves the governing equations by modelling both the large and the small eddies, taking a time-average of variables. As consequence of the average new unknowns, so-called Reynolds stresses arise. Different approaches to evaluate them are: (i) Differentially Reynolds Stress Models (DRSM), (ii) Algebraic Reynolds Stress Models (ARSM), and (iii) Eddy Viscosity Models (EVM) [1].

Although EVM models assuming a linear relation between the turbulent stresses and the mean rate of strain

* Corresponding author. Tel.: +34 93 739 8192.
E-mail address: cttc@cttc.upc.edu (A. Oliva).

0017-9310/$ - see front matter © 2007 Elsevier Ltd. All rights reserved.
doi:10.1016/j.ijheatmasstransfer.2007.02.015

Nomenclature

B	nozzle width
$C_{\epsilon 1}$, $C_{\epsilon 2}$, C_μ	turbulent model constants/function
C_f	skin friction coefficient
c_p	specific heat
D_h	hydraulic diameter
D, E	turbulent model extra terms
f_1, f_2, f_μ	damping functions
H	step height, height of jet discharge above plate
I	turbulence intensity
k	turbulent kinetic energy
l_e	characteristic length scale
Nu	Nusselt number
P_k	production of k due to shear stress
Pr	Prandtl number
Re_τ	friction Reynolds number
Re_θ	Reynolds number based on momentum thickness
Re_H	Reynolds number based on step height
$\overline{S_{ij}}$	mean rate of strain tensor
St	Stanton number
$\overline{T}$	mean temperature
t	time
$\bar{u}_i$	mean velocity
$\overline{u_i'u_j'}$, $\overline{u'u'}$, $\overline{v'v'}$, $\overline{w'w'}$, $\overline{u'v'}$	Reynolds stresses
$\overline{u_i'T'}$	turbulent heat flux
$\bar{p}$	mean pressure
$\overline{W_{ij}}$	mean vorticity tensor
Y_c	Yap correction
y^+	dimensionless distance to the nearest wall

Greek symbols

α^*, β, β^*, β_k, γ_k	turbulent model constants
δ_{ij}	Kronecker delta
ϵ	dissipation rate of k
$\tilde{\epsilon}$	isotropic dissipation rate of k
κ	von Karman's constant = 0.41
λ	thermal conductivity
μ	dynamic viscosity
μ_t	eddy or turbulent viscosity
ρ	density
σ_k, σ_ϵ, σ_ω	turbulent model constants
τ	time scale
ω	specific dissipation rate of k
x_i	Cartesian coordinate in the i-direction

Subscripts

i	i-direction
in	inlet
out	outlet

tensor are extensively used, they present limitations such as isotropy, no-prediction of secondary motions in non-circular ducts, boundary-layer separation, erroneous predictions of the production of turbulence in strong strain fields, etc. In the last few years, with the even-increasing computational capacity, new proposals to overcome many of these deficiencies have started to find their way. Thus, algebraic or non-linear relations can be used to determinate the Reynolds (turbulent) stress tensor without introducing any additional differential equation. Most of these models are or will be incorporated into computational tools and there is no sufficient clarity about which model behaves better even in basic situations with different flow structure. Therefore, systematic studies to establish their properties, numerical performance and spatial requirement in basics and widely studied flows are required.

The main goal of this work is to contribute in an effort to provide conclusions about accuracy, convergence, predictive realism, advantages and shortcomings in the use of explicit algebraic Reynolds stress and linear/non-linear eddy-viscosity models. Furthermore, the effect of using ϵ or ω as length scale variable in the simulated configurations is also studied.

Three basic and intensively investigated configurations, which present different flow structure, are numerically studied. The first case tested is one of the best studied situations: a fully developed turbulent flow in a plane channel [2]. The second case is the flow in a backward facing step, that has a more complex flow structure due to separation and recirculation phenomena [3]. The third case is the flow in an impinging slot jet, which presents a very complex structure despite its relatively simple geometry, involving stagnation, recirculation and adverse pressure zones [4]. The first case serves as a baseline test, and the second and third cases are representative of situations where non-linear and explicit algebraic relations should improve the results due to their characteristics.

Conclusions are extracted after the application of two processes to the studied flows. Firstly, a verification procedure based both on the generalised Richardson extrapolation and the Grid Convergence Index (GCI) is applied to the numerical solutions obtained [5]. Once credibility of the numerical results is assured, the mathematical models are validated by comparison with experimental data and/or DNS results from the literature.

2. Mathematical formulation

2.1. Governing equations

The time-averaged governing equations (continuity, momentum and energy) for incompressible Newtonian fluids, assuming negligible body forces, heat friction, and radiative effects; may be written as follows:

$$\frac{\partial \bar{u}_i}{\partial x_i} = 0 \tag{1}$$

$$\frac{\partial(\rho\bar{u}_i)}{\partial t} + \frac{\partial(\rho\bar{u}_j\bar{u}_i)}{\partial x_j} = -\frac{\partial \bar{p}}{\partial x_i} + \frac{\partial}{\partial x_j}(2\mu\overline{S_{ij}} - \rho\overline{u_i'u_j'}) \tag{2}$$

$$\frac{\partial(\rho\overline{T})}{\partial t} + \frac{\partial(\rho\bar{u}_i\overline{T})}{\partial x_i} = \frac{\partial}{\partial x_i}\left(\frac{\lambda}{c_p}\frac{\partial \overline{T}}{\partial x_i} - \rho\overline{u_i'T'}\right) \tag{3}$$

where $\overline{S_{ij}} = \frac{1}{2}\left(\frac{\partial \bar{u}_i}{\partial x_j} + \frac{\partial \bar{u}_j}{\partial x_i}\right)$. The Reynolds stress tensor ($\overline{u_i'u_j'}$) and the turbulent heat flux ($\overline{u_i'T'}$) are the new unknown terms that appear in the averaging process and they need to be modelled. The models employed here are described below.

2.2. Turbulence models

Three types of RANS models are used in this study in order to calculate Reynolds stresses: explicit algebraic Reynolds stress models (EARSM), non-linear eddy-viscosity models (NLEVM), and linear eddy-viscosity models (LEVM). In the context of two-equation turbulence models, the solution of a set of equations to account for the transport of some turbulent quantities, specifically the turbulent kinetic energy rate per unit mass (k) (Eq. (4)), and some length-scale determining equation, such as the dissipation rate (ϵ) (Eq. (5)) or the specific dissipation rate (ω) (Eq. (6)), amongst others [6], is required

$$\frac{\partial(\rho k)}{\partial t} + \frac{\partial(\rho\bar{u}_i k)}{\partial x_i} = \frac{\partial}{\partial x_i}\left[\left(\mu + \frac{\mu_t}{\sigma_k}\right)\frac{\partial k}{\partial x_i}\right] + P_k - \rho Dis \tag{4}$$

$$\frac{\partial(\rho\tilde{\epsilon})}{\partial t} + \frac{\partial(\rho\bar{u}_i\tilde{\epsilon})}{\partial x_i} = \frac{\partial}{\partial x_i}\left[\left(\mu + \frac{\mu_t}{\sigma_\epsilon}\right)\frac{\partial \tilde{\epsilon}}{\partial x_i}\right] + f_1 C_{\epsilon 1}\frac{\tilde{\epsilon}}{k}P_k - f_2 C_{\epsilon 2}\rho\frac{\tilde{\epsilon}^2}{k} + E + Y_c \tag{5}$$

$$\frac{\partial(\rho\omega)}{\partial t} + \frac{\partial(\rho\bar{u}_i\omega)}{\partial x_i} = \frac{\partial}{\partial x_i}\left[\left(\mu + \frac{\mu_t}{\sigma_\omega}\right)\frac{\partial \omega}{\partial x_i}\right] + \alpha\frac{\omega}{k}P_k - \beta\rho\omega^2 \tag{6}$$

$$\mu_t = C_\mu f_\mu \frac{\rho k^2}{\epsilon} = \alpha^*\frac{\rho k}{\omega} \tag{7}$$

where $P_k = -\rho\overline{u_i'u_j'}(\partial\bar{u}_i/\partial x_j)$; $Dis = \epsilon$ for k–ϵ models; $Dis = \beta^*\omega k$ for k–ω models; and $\tilde{\epsilon} = \epsilon - D/\rho$.

For details about damping functions and closure coefficients of each model see Appendix A.

2.2.1. Linear eddy viscosity models

These kind of models assume the Boussinesq hypothesis [1], where the Reynolds stress is linearly related to the mean rate of strain. The resulting expression can be written as follows:

$$\rho\overline{u_i'u_j'} = \frac{2}{3}\rho k\delta_{ij} - 2\mu_t\overline{S_{ij}} \tag{8}$$

In the present work four linear models are taken into account: IL (Ince–Launder [7]), GPC(Goldberg–Peroomian–Chakravarthy [8]), WX (Wilcox [6]) and WXT (Wilcox [9]). The IL and GPC models use ϵ as dissipation variable, while WX and WXT models use ω.

2.2.2. Non-linear and explicit algebraic models

In these models, the Reynolds stress tensor is calculated using algebraic expressions based on the weak-equilibrium assumption and including terms up to third order in the constitutive relation in function of mean velocity gradients [10].

While both the EARSM and the NLEVM models have similar functional forms, their development follow different paths. In NLEVM the coefficients in the relation of Reynolds stresses are calibrated for some representative flows and they are based on some physical constraints [10]. On the other hand, in EARSM the coefficients appearing in the tensorial expansion are consistent with the differential Reynolds stress model (DRSM) which it is derived [11].

The general expression for $\overline{u_i'u_j'}$ in both EARSM and NLEVM can be written as follows:

$$\begin{aligned}\frac{\overline{u_i'u_j'}}{k} = {} & \frac{2}{3}\delta_{ij} - 2C_\mu^* f_\mu^*\mathbf{S} + \beta_1\left(\mathbf{S}^2 - \frac{1}{3}[\mathbf{S}^2]I\right) + \beta_2(\mathbf{WS} - \mathbf{SW}) \\ & + \beta_3\left(\mathbf{W}^2 - \frac{1}{3}[\mathbf{W}^2]I\right) - \gamma_1[\mathbf{S}^2]\mathbf{S} - \gamma_2[\mathbf{W}^2]\mathbf{S} \\ & - \gamma_3\left(\mathbf{W}^2\mathbf{S} + \mathbf{SW}^2 - [\mathbf{W}^2]\mathbf{S} - \frac{2}{3}[\mathbf{WSW}]I\right) \\ & - \gamma_4(\mathbf{WS}^2 - \mathbf{S}^2\mathbf{W})\end{aligned} \tag{9}$$

where $\overline{W_{ij}} = \frac{1}{2}\left(\frac{\partial \bar{u}_i}{\partial x_j} - \frac{\partial \bar{u}_j}{\partial x_i}\right)$; $\mathbf{S} = \tau(\overline{S}_{ij})$; $\mathbf{W} = \tau(\overline{W}_{ij})$; τ is k/ϵ or $1/\omega$; $I = \delta_{ij}$ and $[\mathbf{M}]$ represents the trace of matrix $\mathbf{M}$.

Two features can be observed in Eq. (9). Firstly, terms associated with coefficients γ_3 and γ_4 disappear in 2D incompressible flows. Secondly, the expression reduces to Eq. (8) when β_k's and γ_k's coefficients are zero.

In this type of formulation, four representative models are implemented: CLS-NLEVM [10], AMGS-EARSM [12], LAR-NLEVM [13] and ARG-EARSM [14]. CLS and AMGS models use k–ϵ, whereas LAR and ARG models use k–ω platform.

The coefficients in the general expression (Eq. (9)) can be found in Appendix A. Table 1 indicates which terms of Eq. (9) are taken into account in the models used.

2.2.3. Turbulent heat flux

In the present study the simple linear eddy diffusivity approach is used for the computation of the turbulent heat flux. It can be written as

$$\rho\overline{u_i'T'} = -\frac{\mu_\tau}{\sigma_T}\frac{\partial T}{\partial x_i} \tag{10}$$

Table 1
Terms appearing in the general stress–strain relationship (Y = yes, N = no)

Model	β_1	β_2	β_3	γ_1	γ_2
LEVM	N	N	N	N	N
AMGS-EARSM [12]	Y	Y	N	N	N
CLS-NLEVM [10]	Y	Y	Y	Y	Y
LAR-LEVM [13]	N	Y	N	N	N
ARG-EARSM [14]	Y	Y	N	N	N

where a constant turbulent Prandtl number $\sigma_T = 0.9$ is assumed for all the turbulence models studied in this work.

3. Numerical procedure

3.1. Solution method

The governing partial differential equations are converted into algebraic ones by means of fully implicit finite volume techniques. They are solved on a structured and staggered grid intensified using a tanh-like function where necessary [15]. The set of equations is solved in a segregated manner using a pressure based method, of the SIMPLE family, to couple the velocity and pressure fields [16]. Central differences are employed for the evaluation of diffusion terms while convective terms are discretized using upwind, power law [16] or high order SMART [17] schemes. The latter scheme has not been applied to the turbulence variables (k, ϵ, ω) due to instability problems. A multi-grid iterative solver is used to solve the algebraic linear system of equations [18].

The addition of higher order terms in the constitutive relation for turbulent stresses has further implications in convergence. Then, an artificial eddy viscosity is used to introduce as many terms as possible in the diffusive terms of the momentum equations [19]. Thus, only the remaining terms of the constitutive relation are maintained explicitly in the source term.

In the k, ϵ or ω equations the source term is linearised in order to avoid negative values. All production terms are included in the source term (right side), while dissipation terms are transferred to the left hand side of the discretized equation [15].

3.2. Verification of numerical solutions

In order to verify the numerical solutions obtained, a post-processing procedure based on the generalised Richardson extrapolation for *h-refinement* studies and on the Grid Convergence Index (GCI), has been used in order to establish a criterion about the sensitivity of the simulation to the computational model parameters that account for the discretization: the mesh spacing and the order of accuracy of the numerical solution. Local estimators of the error band, where the independent grid solution is expected to be contained (uncertainty due to discretization, GCI), and the observed order of accuracy (p) are calculated at the grid nodes where their evaluation has been possible. These grid nodes are named *Richardson nodes*. Global values of GCI and p are calculated by means of a volumetric averaging. An estimation is considered to be credible when the global observed order of accuracy p approaches the theoretical value, and when the number of *Richardson nodes* is high enough. See [5] for details.

4. Test cases

4.1. Plane channel flow

This flow constitutes one of the most basic confined cases due to its simplicity and parabolic flow structure, where the shear stress is the most important characteristic. Some examples of works found in literature studying channel flow are herewith summarised. Heyerichs and Pollard [20] studied several turbulence models in a channel at high Reynolds and presented results for Nusselt number, skin-friction coefficient and log-law for dimensionless stream velocity. Craft et al. [10] applied their model to a channel with two Reynolds numbers, and compared it with results from DNS. Apsley and Leschziner [21] first used the NLEVM model in a channel, and Moser et al. [2] studied the channel by means of DNS for the same Reynolds numbers considered in this study.

In general, this flow is used as a basic case to check the correct implementation or to fit the constants of turbulence models. Three different friction Reynolds numbers based on half channel height and friction velocity (u_τ), are herewith selected: $Re_\tau = 180$, $Re_\tau = 395$ and $Re_\tau = 590$. The fluid is air ($Pr = 0.71$).

In Fig. 1a, the physical domain and boundary conditions are shown. The Reynolds number (Re_{D_h}) based on hydraulic diameter (D_h) and inlet mean velocity (u_{in}) is calculated using $Re_\tau \approx 0.09 Re_{D_h}^{0.88}$ [1]. The specific turbulent kinetic energy dissipation (ω_{in}) is evaluated from ϵ_{in} with the relation $\omega_{in} = \epsilon_{in}/\beta^* k_{in}$ (where β^* is a model constant). At the exit, a pressure outflow boundary condition is imposed, and a null gradient in x-direction of scalar variables (T, k, ϵ or ω) is assumed.

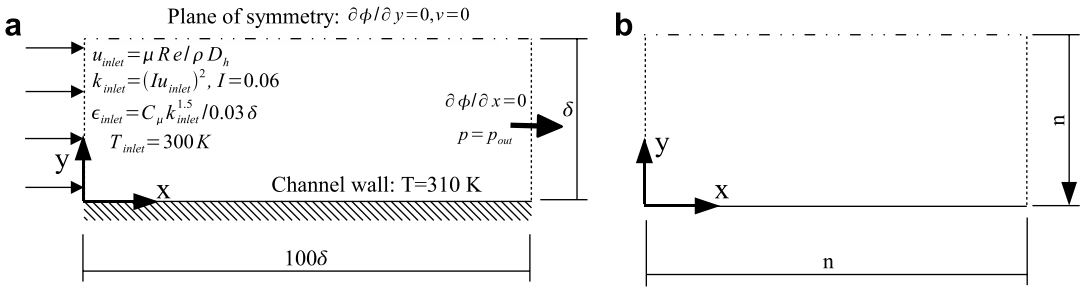

Fig. 1. Channel flow test case. (a) Geometry and boundary conditions. (b) Computational domain, number of control volumes (n), and mesh distribution in x and y directions. Solid triangle indicates direction of mesh concentration.

4.1.1. Verification

Although the *h-refinement* study has been carried out for all models and Reynolds numbers, only results for the IL ($k\epsilon$-LEVM) model at $Re_\tau = 590$ using upwind scheme for convective terms are presented in Table 2. The grid distribution is shown in Fig. 1b. The number of control volumes is represented by the parameter n, e.g. when $n = 40$ it expresses the problem is solved on 40×40 control volumes (cv's). The mesh is intensified near solid wall, which is indicated in the figure with a solid triangle. The grids employed for verification correspond to $n = 20$, 40, 80, 160 and 320. Taking advantage of symmetry, only half of the channel is simulated.

As can be observed in Table 2, the Richardson nodes are sufficiently large for the three estimations shown (more than 88%). The observed order of accuracy p also agrees with its theoretical value, from 1 to 2, considering the upwind scheme and the almost parallel flow structure. The reduction from mesh to mesh of GCI values shows a tendency to an asymptotic value (i.e. a grid independent solution). Similar results are observed for the other models and Reynolds number. Therefore, they are not presented. The SMART scheme has also been used obtaining a similar accuracy. According to this study, the fourth grid is used in the comparative study.

4.1.2. Validation and comparative study

The turbulence models tested are validated with DNS results obtained by Moser et al. [2] for a detailed comparison of both the mean velocity and the turbulent stresses. The Nusselt number Nu is compared versus Dittus–Boelter correlation ($Nu = 0.023 Re_{D_h}^{0.8} Pr^{0.4}$) (cited in [22]). The skin-friction factor C_f is compared in the fully developed region and is obtained from: $1 = 2\sqrt{C_f}[2\log(2Re_{D_h}\sqrt{C_f}) - 0.8]$ (cited in [22]).

Results for Nu and C_f are presented in Table 3. In general, LEVM, NLEVM and EARSM exhibit a proper performance compared to the empirical correlations. Only GPC ($k\epsilon$-LEVM), WX ($k\omega$-LEVM) and WXT ($k\omega$-LEVM) models show poor solutions for C_f. The best results are obtained with CLS ($k\epsilon$-NLEVM) model.

The Nusselt number is better predicted by AMGS ($k\epsilon$-EARSM) model followed by LAR ($k\omega$-NLEVM) model. Thus, comparing these parameters in this configuration, NLEVM and EARSM perform better than LEVM. Nevertheless, the model that most accurately predicts the C_f is not the same as the one which better predicts the Nu.

Dimensionless turbulent kinetic energy and turbulent normal stream-wise stress maps ($\overline{u'u'}$) for $Re_\tau = 395$ are plotted in Fig. 2. Results are compared to DNS data [2]. The WXT ($k\omega$-LEVM) model gives the most accurate prediction of k peak. CLS ($k\epsilon$-NLEVM) also shows reasonable results for this variable, while the rest of models underpredict it. This deficiency is more evident in the case of WX ($k\omega$-LEVM), ARG ($k\omega$-EARSM) and AMGS ($k\epsilon$-EARSM) models in the region near the wall ($y^+ < 70$) for all Reynolds numbers.

However, as can be seen in Figs. 2 and 3, proper results for k not always mean an adequate prediction of normal

Table 2
Channel flow case, results from grid refinement study

Grids (n)	$u^* = u/u_{in}$			$k^* = k/k_{in}$			$T^* = T/T_{in}$		
	R_n (%)	p	GCI* (%)	R_n (%)	p	GCI* (%)	R_n (%)	p	GCI* (%)
20/40/80	98	1.5	1.5e−01	96	1.6	3.3e+00	98	1.4	2.2e+00
40/80/160	97	1.7	4.8e−02	96	1.8	9.2e−01	97	1.6	6.0e−01
80/160/320	89	1.7	2.7e−02	93	1.9	2.5e−01	93	1.6	3.1e−01

$Re_\tau = 590$ and IL model. Richardson nodes (R_n), global order of accuracy (p) and global uncertainty (GCI*). The global uncertainty is normalised using all of the inlet values.

Table 3
Channel flow, validation

Model	$Re_\tau = 180$				$Re_\tau = 395$				$Re_\tau = 590$			
	Nu	(%)	$C_f \times 10^3$	(%)	Nu	(%)	$C_f \times 10^3$	(%)	Nu	(%)	$C_f \times 10^3$	(%)
Correlation	35.00	–	7.484	–	71.40	–	5.994	–	102.97	–	5.390	–
IL	30.54	−12.74	7.210	−3.66	64.55	−9.59	5.774	−3.67	93.48	−10.14	5.283	−1.98
GPC	38.87	11.06	8.629	15.29	76.19	6.71	6.820	13.78	107.82	5.18	6.034	11.94
CLS	30.66	−12.40	7.478	−0.08	66.28	−7.17	5.953	−0.68	96.05	−7.39	5.379	−0.20
AMGS	35.42	1.20	7.950	6.22	70.42	−1.37	6.331	5.62	101.06	−2.04	5.695	5.65
WX	40.42	15.48	8.967	19.81	72.26	1.20	6.867	14.56	108.84	5.7	6.075	12.71
WXT	42.11	20.31	9.311	24.41	78.23	9.56	6.974	16.34	108.66	5.52	6.126	13.65
LAR	36.18	3.37	8.083	8.00	68.90	−3.5	6.156	2.70	97.16	−5.64	5.434	0.82
ARG	39.82	13.77	8.839	18.10	73.42	2.83	6.541	9.12	106.22	3.15	5.948	10.35

Nusselt number, skin-friction coefficient and relative discrepancy with empirical correlations [22].

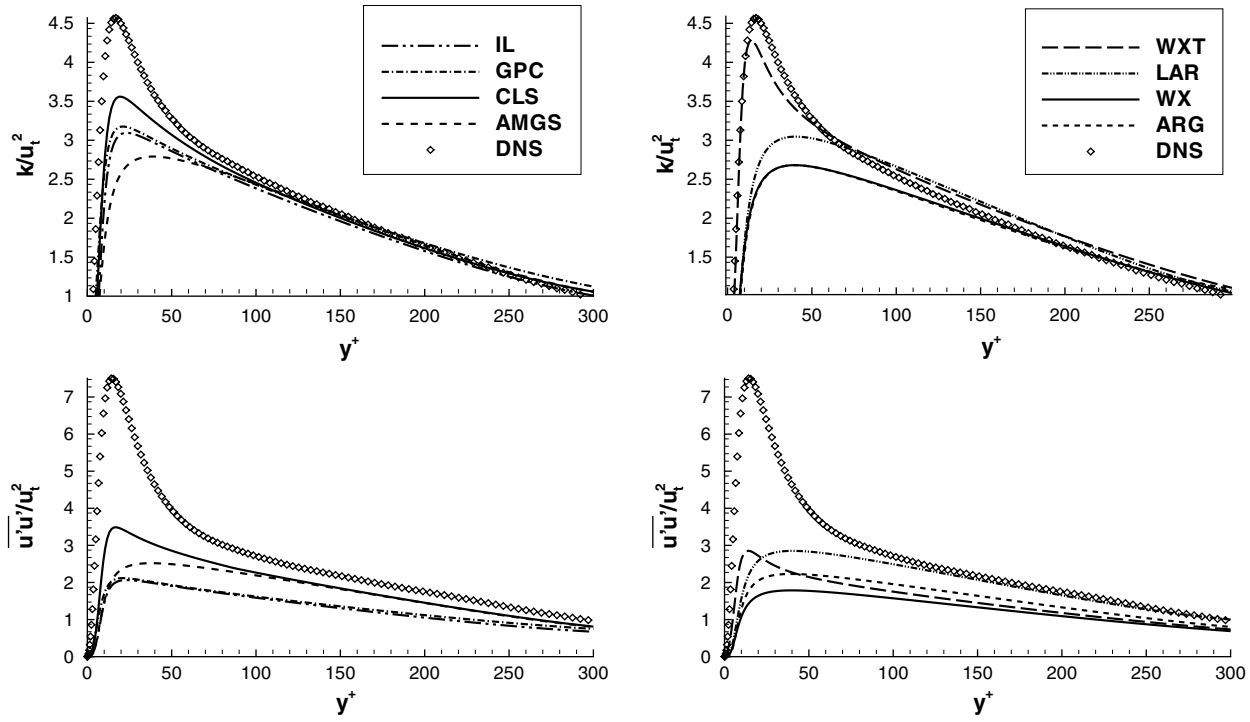

Fig. 2. Channel flow. Turbulent kinetic energy and normal Reynolds stress in x-direction, $Re_\tau = 395$.

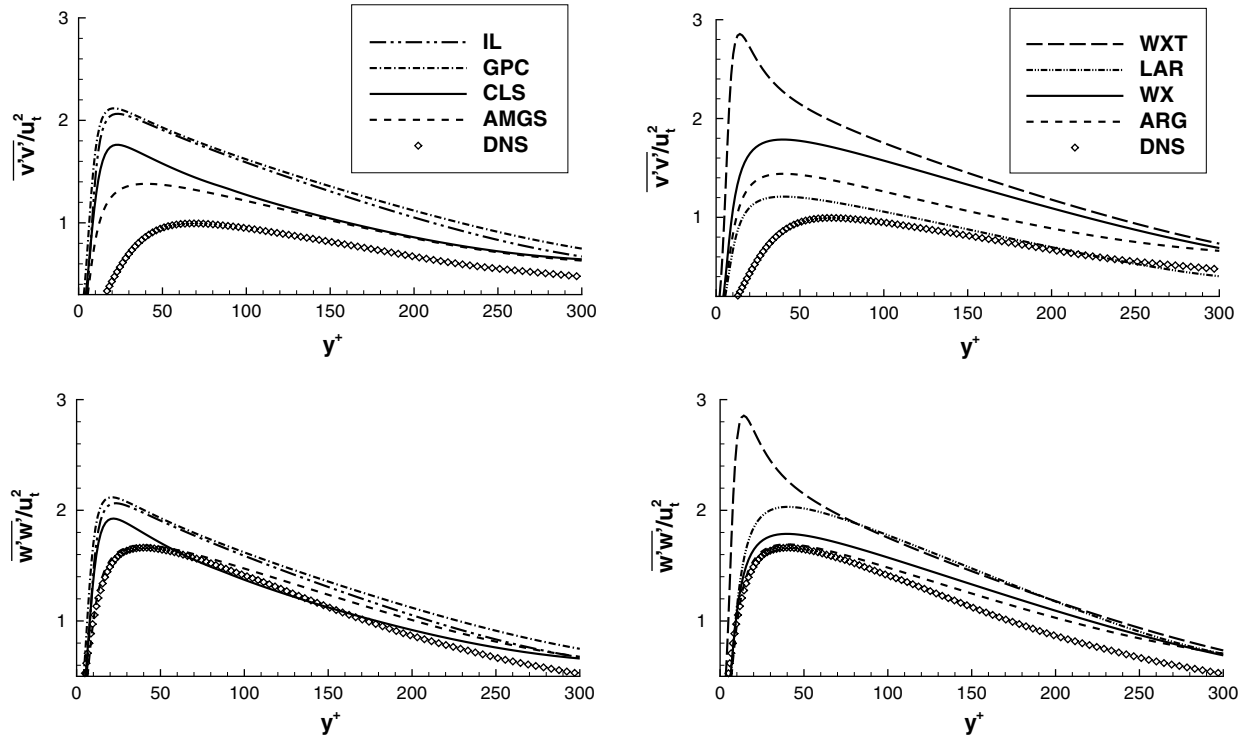

Fig. 3. Channel flow. Normal Reynolds stresses in y- and z-directions, $Re_\tau = 395$.

turbulent stresses. This is more notable in the case of LEVM models. As consequence of the isotropy assumption, they incorrectly predict similar profiles for all of them. Such situation is clearly illustrated in the WXT ($k\omega$-LEVM) model. It gives an adequate level for the turbulent kinetic energy and tends to reproduce the $\overline{u'u'}$ peak. Nevertheless, it poorly predicts $\overline{v'v'}$ and $\overline{w'w'}$. A superior accomplishment of the WXT ($k\omega$-LEVM) model for k and $\overline{u'u'}$ is darkened with its poor performance in the estimation of the other normal stresses.

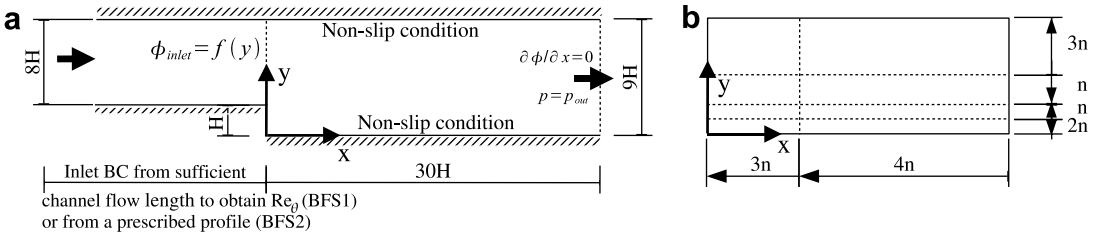

Fig. 4. Backward facing step flow (BFS). (a) Geometry and boundary conditions. (b) Computational domain, number of cv's (n), and mesh distribution in x- and y-directions. Solid triangles indicate direction of mesh concentration.

Taking these results into account, the use of NLEVM is beneficial. As result of the predicted anisotropy level, an acceptable solution of turbulent normal stresses is presented.

When NLEVM are compared with EARSM, it is important to keep in mind that the first ones are tuned for this kind of flows. Thus it is expected that they perform adequately. Nevertheless, NLEVM models do not properly reproduce any turbulent normal stress. Therefore, empirical coefficients in the constitutive relation should be adjusted to predict higher anisotropy levels. In addition, it is remarkable that EARSM lead to acceptable results with only one damping function, whereas the other models require up to four (f_μ, f_2, E and D) when k–ϵ platform is used.

4.2. Backward facing step flow (BFS)

This configuration is usually used to compare the performance of turbulence models for recirculating, re-attaching and separated turbulent boundary-layer flows. Moreover, it includes shear-layer mixing process and a region with adverse pressure gradient.

Several experimental studies have been reported in the last decades. For example, those carried out by Eaton and Johnston [23], Vogel and Eaton [24], Kim et al. [25] and Driver and Seegmiller [3]. Most of them have then been numerically simulated. For example, Heyerichs and Pollard [20] studied the configuration of Vogel and Eaton [24], and presented results for global parameters i.e. Nusselt and Stanton number for several LEVM. Park and Sung [26] applied a new model to this case and compared mean velocity, normal turbulent stresses at two positions and skin friction coefficient along step wall. Thangam and Speziale [27] used the experimental data by Kim et al. [25] to evaluate standard k–ϵ and NLEVM models with different approaches near solid walls. They presented results for mean velocity, shear stress and global variables.

The experimental configuration by Driver and Seegmiller [3], hereafter referred as BFS1, is studied in this work. The expansion ratio (outlet/inlet height) is 1.125. The inlet boundary conditions ($u_{in}(y)$, $v_{in}(y)$, $k_{in}(y)$, $\epsilon_{in}(y)$ or $\omega_{in}(y)$) correspond to the numerical solution of a channel flow at the section where $Re_\theta = 5000$. The turbulence model used to generate the above mentioned inlet boundary condition was the IL-LEVM for k–ϵ models and WXT-LEVM for k–ω based models. At the exit a pressure outflow boundary condition is imposed (see Fig. 4a for details). The free stream velocity in the channel, $u_{ref} = 44.2$ m/s, is used for non-dimensionalization purposes.

In this flow, inlet boundary condition is crucial for the development of the recirculation zone and, as a consequence, for a critical evaluation and comparison of turbulence models. Therefore, in [28] a study has been carried out to compare different options to obtain it.

Furthermore, the experimental setup used by Vogel and Eaton [24] is analised here for a $Re_H = 28\,000$ (hereafter referred as BFS2). Geometry and boundary conditions are imposed according to [20]. The inlet boundary condition corresponds to a boundary layer with $\delta/H = 1.1$, $u_{in} = u_{ref}(y/\delta)^{1/7.05}$, $v_{in} = 0$, $k_{in} = C_\mu^{-0.5} l^2 (\partial u_{in}/\partial y)^2$, $l = \min[\kappa y, 0.09\delta]$, $\epsilon_{in} = C_\mu k^2 (l^2 \partial u_{in}/\partial y)^{\frac{\mu}{1}}$ and $T_{in} = 300$ K. For values of $y > \delta$, $u_{in} = u_{ref} = f(Re_H)$, $v_{in} = 0$, $k_{in} = 1.5(Iu_{ref})^2$, $\epsilon_{in} = C_\mu k_{in}^{1.5}/(0.09\delta)$ and $T_{in} = 300$ K are imposed. Non-slip condition and $q_w = 270$ W/m^2 are used at the bottom wall, and at the top boundary main stream values are fixed.

4.2.1. Verification

Results of the *h-refinement* study for u, v and k are presented in Table 4 for BFS1. Convective terms of Eqs. (2) and (3) are discretized with SMART scheme while in Eqs. (4)–(6) power-law scheme is used.

For this case the grid is represented by the parameter n (number of cv's) in Fig. 4b. The mesh has been intensified near the solid walls and the step, as it is indicated with solid triangles in the figure. Five grids have been used $n = 3$, 6, 12, 24 and 48 (i.e. meshes of 21×21, 42×42, 88×88, 176×176 and 352×352 cv's respectively). For these meshes, the first node nearest to the wall is located at $y^+ = 12$, 6.5, 3.8, 1.2 and 0.6 respectively. Also, for completeness, some models are applied using a sixth mesh of $n = 96$ (704×704 cv's). All models exhibit similar trends and only three of them are herewith presented.

The number of Richardson nodes (R_n) in the last two set of grids is over 80%. The order of accuracy (p) is also within the expected theoretical range when the mentioned schemes are used in reattaching flows. However, some exceptions have been found for the set of grids with $n = 6/12/24$, and are explained below. Furthermore, the first set of meshes ($n = 3/6/12$) has displayed neither an adequate R_n nor a p.

Table 4
BFS1, results from grid refinement study

Grids (n)	$u^* = u/u_{in}$			$v^* = v/u_{in}$			$k^* = k/k_{in}$		
	R_n (%)	p	GCI* (%)	R_n (%)	p	GCI* (%)	R_n (%)	p	GCI* (%)
CLS model									
3/6/12	45	0.1	7.2e+00	49	0.6	2.5e−01	74	1.2	2.3e+01
6/12/24	90	0.5	5.2e−01	87	0.6	1.0e−01	87	1.1	1.2e+01
12/24/48	96	1.2	7.7e−02	93	1.2	2.0e−02	94	1.4	3.3e+00
WX model									
3/6/12	54	0.7	1.8e+00	52	1.0	1.4e−01	88	2.9	1.8e+01
6/12/24	87	0.9	6.1e−01	82	0.6	1.7e−01	90	1.7	1.8e+01
12/24/48	93	1.5	9.9e−02	91	1.3	2.9e−02	93	1.8	4.9e+00
24/48/96	92	2.3	1.1e−02	93	2.3	2.7e−03	92	2.4	4.3e−01
LAR model									
3/6/12	57	0.4	2.9e+00	56	0.8	3.2e−01	89	3.0	1.0e+01
6/12/24	89	1.5	2.0e−01	84	1.0	7.7e−02	91	1.9	6.9e+00
12/24/48	91	1.8	4.5e−02	92	1.6	1.6e−02	88	1.9	2.1e+00

Richardson nodes (R_n), global order of accuracy (p) and global uncertainty (GCI*). The global uncertainty is normalised using inlet values.

The results from the second set of grids reflect the importance of y^+ parameter (dimensionless distance to the nearest wall) in the correct performance of the models, specially of LEVM using k–ω platform. Due to the boundary condition used for these models, y^+ corresponding to the first inner node from the wall should be lower than 2.5 [6]. The grids with $n = 3$, 6 and 12 are above this limit, while the fourth mesh ($n = 24$) presents a y^+ below it. Thus, there is an oscillation between results of these grids and the asymptotic behaviour is broken. A similar trend is observed in k–ϵ models, although their boundary condition shows less sensitivity to this distance.

For BFS2 a similar grid to that of BFS1 is used, but instead of the mesh concentration applied in BFS1 near the top wall, a uniform distribution is occupied in BFS2. For this case an analogous *h-refinement* procedure is also applied. Results of the study are correct and comparable to those of BFS1. For example, for the set of meshes with $n = 6$, 12 and 24 using WXT ($k\omega$-LEVM) a number of $R_n > 75\%$ is achieved for all variables. Furthermore, GCI's values of 1.5%, 0.48% and 0.84% are obtained for velocity, temperature and turbulent kinetic energy respectively. Therefore, extensive results of the *h-refinement* study for BFS2 are not included in this work.

Summarising, it is found that the uncertainty due to discretization (GCI) for the last grid ($n = 48$) is small enough as to consider its results as credible. Thus, the fifth mesh is used for comparative purposes.

4.2.2. Validation and comparative study

4.2.2.1. Reattachment point. One of the common quantities used to evaluate the performance of a turbulence model in the backward-facing step configuration, is the reattachment length of the flow separation.

For BFS1, Table 5 shows that LEVM under-predicts the reattachment point (X_r/H), with the exception of WXT ($k\omega$-LEVM) model. The shortest length is exhibited by the IL ($k\epsilon$-LEVM) model. Otherwise, the X_r/H calculated with NLEVM and EARSM is a bit longer than experimental data. Due to the under-prediction of turbulence levels in the separated shear layer, AMGS ($k\epsilon$-EARSM) model presents the largest value. Thus, the generation term in Eq. (5) should be increased for a better behaviour of this model in flows with adverse pressure gradients. This conclusion has also been found by other authors [19,21].

For BFS2, results of X_r/H are presented in Table 6. Observing this quantity is seen that higher order models do not improve linear models results. NLEVM and EARSM predict an excessively long recirculation region [24]. Furthermore, this overestimation is more evident in k–ϵ based models, giving an idea about the low level of turbulent mixing predicted by these models in this case.

4.2.2.2. Minimum skin-friction coefficient. Reviewing the differences of the minimum skin-friction coefficient ($C_{f\,min}$) obtained respect to the experimental data, the superiority and advantages of using higher order terms in the constitu-

Table 5
BFS1, validation

Models	IL	GPC	CLS	AMGS	WX	WXT	LAR	ARG	Driver and Seegmiller [3]
X_r/H	5.85	6.13	6.54	6.89	5.87	6.28	6.46	6.316	6.26 ± 0.1
%	−6.55	−2.08	4.47	10.06	−6.23	0.319	3.19	0.895	–
$C_{f\,min} \times 10^3$	1.612	1.405	1.275	1.603	1.244	1.151	0.862	1.081	1.02
%	58.04	37.74	25.00	57.16	21.96	12.84	−15.49	5.98	–

Reattachment point (X_r/H) and minimum skin-friction ($C_{f\,min}$) coefficient. Relative discrepancy (%) with experimental data.

Table 6
BFS2, validation

Models	IL	GPC	CLS	AMGS	WX	WXT	LAR	ARG	Vogel and Eaton [24]
X_r/H	7.42	7.46	8.68	8.34	6.73	7.71	7.87	7.31	6.67
%	11.2	11.8	30.1	20.1	0.90	15.6	18.0	9.6	–
$C_{f\min} \times 10^3$	1.77	1.55	1.38	1.67	1.43	1.25	0.98	1.19	1.14
%	55.3	36.0	21.1	46.5	25.4	9.6	−14.0	4.38	–

Reattachment point (X_r/H) and minimum skin-friction ($C_{f\min}$) coefficient. Relative discrepancy (%) with experimental data.

tive relation is clear (see Table 5 for BFS1 and Table 6 for BFS2). For example, and considering k–ϵ platform, CLS ($k\epsilon$-NLEVM) model gives better results than IL ($k\epsilon$-LEVM) model in both configurations. Moreover, in the case of k–ω platform, LAR ($k\omega$-NLEVM) and ARG ($k\epsilon$-EARSM) models predict the minimum more accurately than WX ($k\omega$-LEVM) model, which is their linear counterpart.

4.2.2.3. Skin friction coefficient at the bottom wall. Figs. 5 and 6 present the comparison of skin-friction coefficient (C_f) at the bottom wall with the experimental data [3] for BFS1. Moreover, for BFS2 it is plotted in Figs. 7 and 8. C_f is usually related with the near-wall characteristics of the turbulence model used. In general, the influence of using higher order terms are more notorious in k–ϵ than in k–ω models (see Figs. 5 and 7). Furthermore, k–ω models have outperformed k–ϵ ones, which is expected due to the better performance of the ω-based models near solid walls. However, the last ones underestimate C_f downstream the redeveloping region in BFS2. Good accordance with the results for the LEVM presented in [20] is shown here for this configuration, i.e. WXT ($k\omega$-LEVM) and IL ($k\epsilon$-LEVM) models.

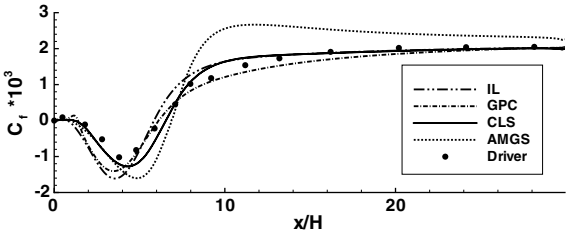

Fig. 5. BFS1. Skin-friction coefficient for k–ϵ models.

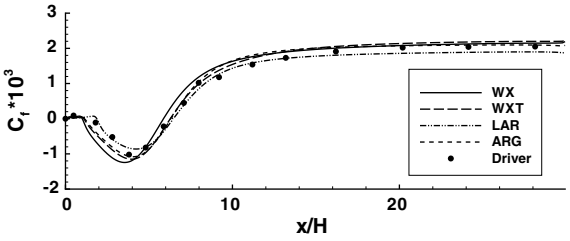

Fig. 6. BFS1. Skin-friction coefficient for k–ω models.

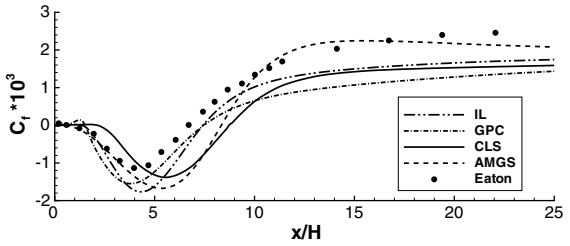

Fig. 7. BFS2. Skin-friction coefficient for k–ϵ models.

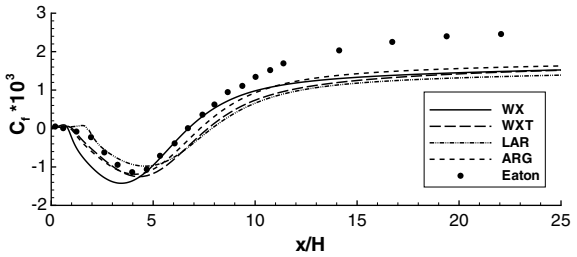

Fig. 8. BFS2. Skin-friction coefficient for k–ω models.

4.2.2.4. Stanton number bottom wall. Stanton number (St) is chosen to evaluate turbulence models performance for the estimation of the heat transfer in BFS2. St profiles together with the corresponding experimental data [24] are presented in Figs. 9 and 10. All k–ω models show good agreement with measurements. Otherwise, k–ϵ models predict dispersed results, being GPC ($k\epsilon$-LEVM) the only model capable of reproducing the experiment [24]. Thus, based on the view of Figs. 9 and 10, benefits of using NLEVM or EARSM are rather limited for this case.

4.2.2.5. Mean velocity BFS1. The predicted mean streamwise velocity profiles at different cross-sections are shown in Fig. 11 along with experimental results [3]. The numerical profiles estimated by all models seem to be in agreement

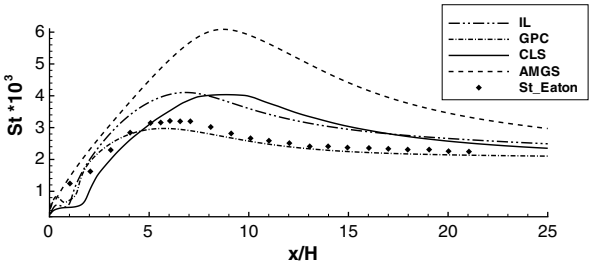

Fig. 9. BFS2. Stanton number for k–ϵ models.

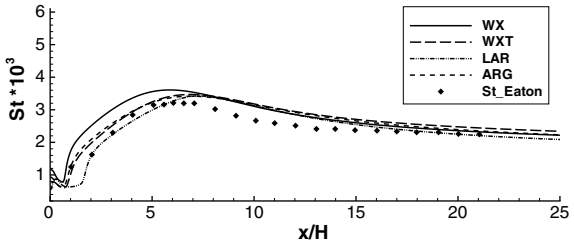

Fig. 10. BFS2. Stanton number for k–ω models.

with the data, except at the bottom wall near the reattachment point.

The k–ω linear models somewhat depart from experimental data away the wall. This departure is larger in the recovery region. Only ARG ($k\omega$-EARSM) reproduces experimental results correctly.

In the redeveloping zone AMGS ($k\epsilon$-EARSM) and LAR ($k\omega$-NLEVM) models present some deviations. These differences remain downstream. Therefore, reviewing this quantity, it can be said there is an inappreciable improvement with the use of higher order terms.

4.2.2.6. Turbulent stresses BFS1. When normal Reynolds stresses are analysed, remarkable differences between models and experimental results are found (see Figs. 12 and 13). LEVM models erroneously predict a value for $\overline{v'v'}$ larger than for $\overline{u'u'}$. This trend is corrected by NLEVM and EARSM models, presenting at least qualitatively correct results due to the addition of higher order terms. Furthermore, Reynolds stresses predictions show that the addition of these terms in the constitutive relation tends to increase $\overline{u'u'}$, but have less effect on the shear stress. Thus, analysing

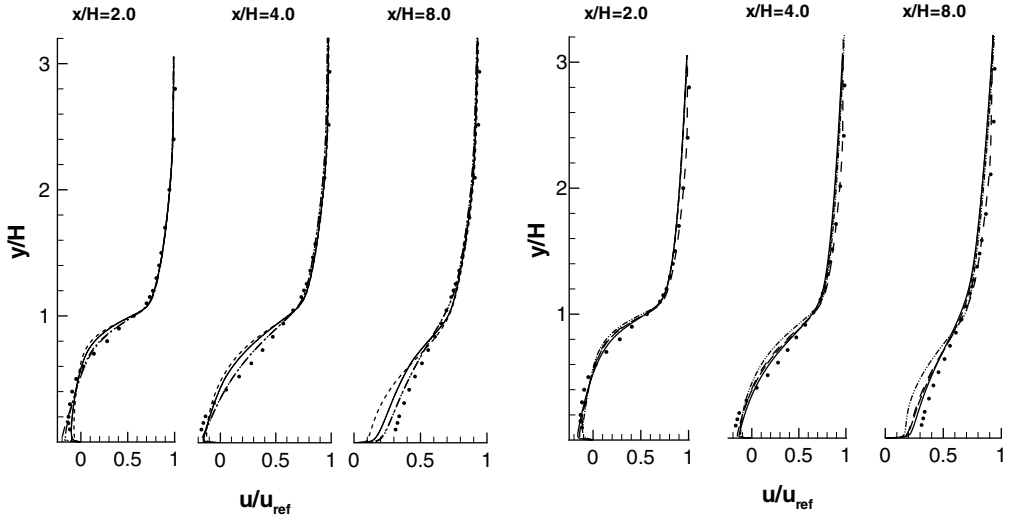

Fig. 11. BFS1. Dimensionless streamwise velocity profiles, left k–ϵ models - ·· - IL, - · - GPC, —- CLS, - - - AMGS, right k–ω models —- WX,– – – WXT, - ·· - LAR, - - - ARG and symbols experiments [3].

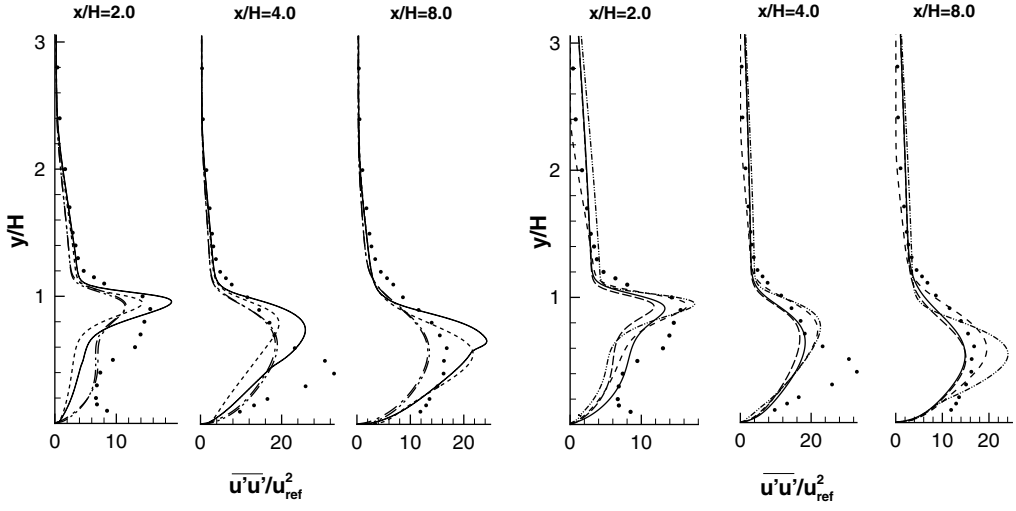

Fig. 12. BFS1. Dimensionless streamwise turbulent stress profiles, left k–ϵ models - ·· - IL, - · - GPC, —-CLS, - - - AMGS, right k–ω models —- WX, – – – WXT, - ·· - LAR, - - - ARG and symbols experiments [3].

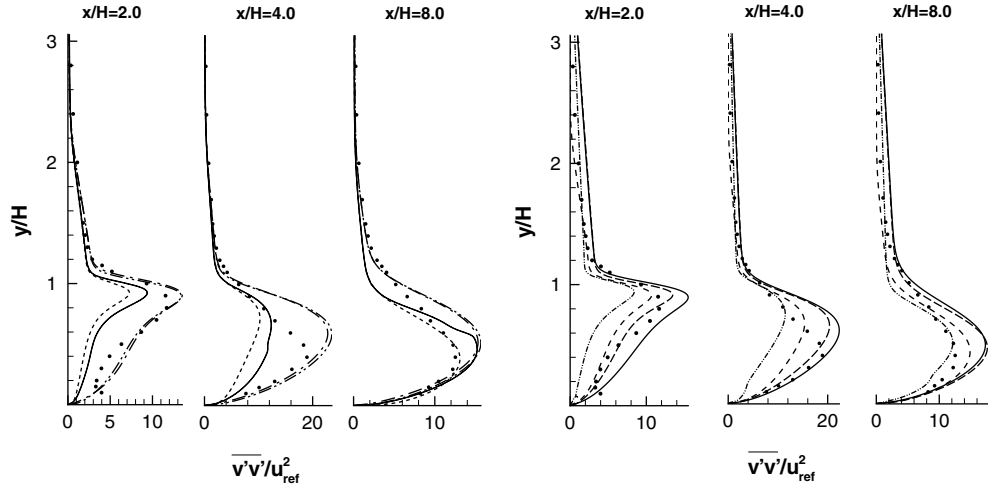

Fig. 13. BFS1. Dimensionless y-direction turbulent stress profiles, left k–ϵ models - ·· - IL, - · - GPC, —- CLS, - - - AMGS, right k–ω models —- WX, – – – WXT, - ·· - LAR, - - - ARG and symbols experiments [3].

these variables the use of NLEVM or EARSM is important.

4.3. Impinging slot jet flow

In spite of its simple geometry, the impinging slot jet presents a complex flow structure with stagnation, recirculation and adverse pressure regions. This case has been chosen to investigate the performance of the models in the presence of normal straining (the flow in the stagnation region is nearly irrotational and a large strain along streamlines is produced) [10,21].

Experimental studies for thermal field have been carried out by Gardon and Akfirat [29] and Van Heiningen [4], among others, for several Reynolds numbers.

Numerical studies were published by Heyerichs and Pollard [20] and Wang and Mujumdar [30], who examined an impinging slot jet at a Reynolds number of 10 000 based on nozzle width and bulk velocity. Seyedin et al. [31] performed other work for various Reynolds numbers and nozzle-to-impingement surface spacing (H/B) ratios. More recently, Shi et al. [32] studied the effect of inlet conditions over the heat transfer.

In this work a single turbulent confined impinging air slot jet is numerically studied at $Re_B = 10\,200$ and $H/B = 2.6$ [4]. Inlet vertical velocity (V_{in}) is obtained from the Reynolds number value. Turbulent kinetic energy (k_{in}) is calculated with an intensity of $I = 0.02$, and the characteristic length used to determine the turbulent kinetic energy dissipation rate (ϵ_{in}) at inlet is $l_e = 0.015^* B$. No-slip condition is imposed at solid walls. At the exit, a pressure boundary condition is used (see Fig. 14a for details). These boundary conditions are the same as the ones used by Heyerichs and Pollard [20].

4.3.1. Verification

Results obtained using the verification procedure based on the Richardson extrapolation are shown in Table 7. Details of the number of grid nodes (represented by the parameter n) and mesh concentration are given in Fig. 14b. The verification study is performed with five levels (grids) of refinement: $n = 3$, 6, 12, 24, 48 (i.e. meshes of 33×21, 66×42, 132×84, 264×168 and 528×336 control volumes respectively). For these meshes, the first node nearest to the wall is located at $y^+ = 8.5$, 3.8, 1.7, 0.85 and 0.42, respectively. Due to symmetry, only half of the flow

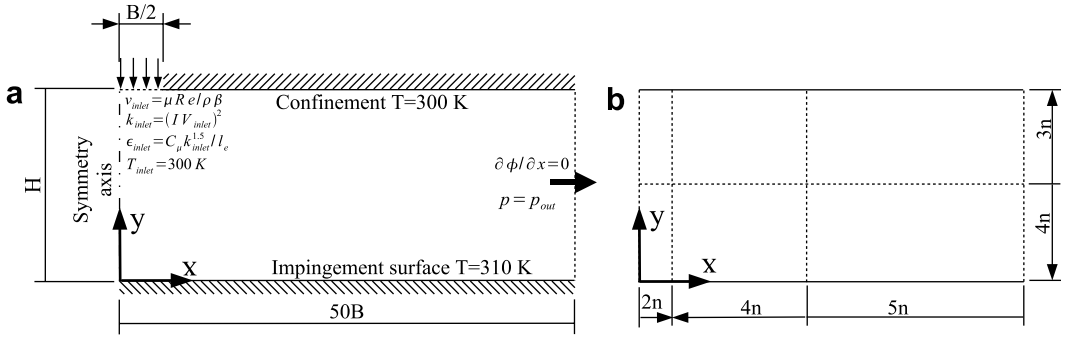

Fig. 14. Impinging jet. (a) Geometry and boundary conditions. (b) Computational domain, number of cv's (n), and mesh distribution in x- and y-directions. Solid triangles indicate direction of mesh concentration.

Table 7
Impinging jet flow case, results from grid refinement study

Grids (n)	u			v			T			k		
	R_n (%)	p	GCI (%)	R_n (%)	p	GCI (%)	R_n (%)	p	GCI (%)	R_n (%)	p	GCI (%)
IL model												
3/6/12	75	0.1	3.0e+02	69	−0.3	1.2e+01	68	1.2	6.8e+00	73	0.4	1.1e+01
6/12/24	83	−0.8	1.8e+02	85	0.1	2.9e+01	77	0.9	8.7e+00	78	0.1	1.6e+02
12/24/48	85	0.7	1.3e+01	84	0.6	2.1e+00	76	1.1	5.4e+00	81	0.7	6.5e+00
AMGS model												
3/6/12	72	1.2	6.5e+00	76	1.0	9.2e−01	72	1.2	7.5e+00	70	1.3	2.0e+00
6/12/24	85	1.1	2.4e+00	68	1.2	5.1e−01	64	2.8	4.0e−01	80	1.6	4.2e−01
12/24/48	89	1.1	1.0e+00	82	1.1	2.1e−01	76	1.5	5.3e−01	83	1.4	2.4e−01
ARG model												
3/6/12	49	1.6	1.1e+00	43	1.5	3.4e−01	57	1.4	3.9e+00	44	2.6	2.0e−01
6/12/24	85	0.4	1.1e+01	83	0.3	3.2e+00	76	0.8	5.0e+00	86	0.4	4.8e+00
12/24/48	78	1.2	9.7e−01	74	1.2	2.8e−01	78	1.2	1.5e+00	76	1.2	5.0e−01

Richardson nodes (R_n), global order of accuracy (p) and global uncertainty (GCI).

domain has been considered. For all variables central difference scheme has been used for diffusive terms and power law scheme for convective ones. Higher order schemes have not been used due to convergence difficulties in the finest grids.

For the third set of grids, $n = 12/24/48$, an asymptotic behaviour with a number of Richardson nodes (R_n) over 70% are obtained for most of the models. The observed order of accuracy (p) is around the unity, which is expected when a combination of central difference and power law schemes are applied. However, for the first two sets ($n = 3/6/12$ and $n = 6/12/24$), the p obtained does not fit its theoretical value. Thus, the results for these two sets can not be considered credible.

It is important to highlight that the *h-refinement* procedure is applicable as long as a smoothness and asymptotic behaviour is presented, a converged solution has been raised and the variable studied is not almost zero. Two exceptions of these requirements have been found in this study:

- WX ($k\omega$-LEVM), WXT ($k\omega$-LEVM) and ARG ($k\omega$-EARSM) models: The same oscillatory behaviour observed in BFS case is presented here in function of the y^+ parameter. However, as it has been pointed out, the last set ($n = 12/24/48$) presents an asymptotic behaviour, making our numerical results credible and ensuring that the mathematical model is adequately solved. As the y^+ corresponding to the nearest grid point to the wall is also lower than 2.5, the restriction for the boundary condition imposed for ω-based models is fulfilled.
- IL ($k\epsilon$-LEVM) and CLS ($k\epsilon$-NLEVM) models: Even though fine grids have been used in the simulation, IL ($k\epsilon$-LEVM) and CLS ($k\epsilon$-NLEVM) models have not shown an asymptotic behaviour in this case. This is demonstrated in the results obtained when the verification procedure is applied (see Table 7). Moreover, results for Nusselt number are presented in Fig. 15. It seems that the results for the finest mesh are still far from the grid independent solution. Therefore, the finest

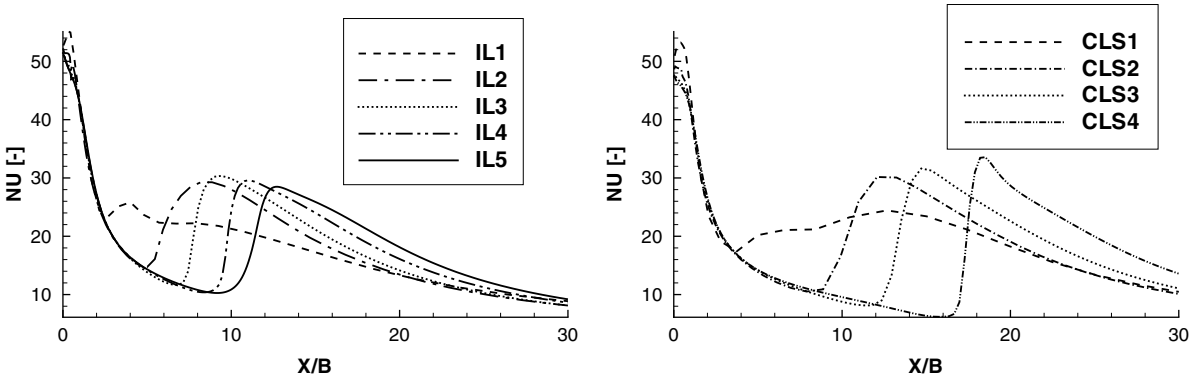

Fig. 15. Impinging jet. Verification: Nusselt number impingement plate for different grids. Left IL model and right CLS model. - - - coarse grid; – · – · – second grid; ···· third grid; – · · – · · – fourth grid; —— finest grid.

converged grid for each model is used in the comparative study, even though asymptotic behaviour has not been completely reached.

In the case of LAR ($k\omega$-NLEVM) model, it has not been possible to reach a sufficiently converged solution for the finest mesh. Thus, the obtained results have not been adequately verified. For this reason, the results presented must be taken with caution for this model.

Apart from the situations explained above, Table 7 shows that at least the fourth mesh is necessary to ensure grid independent solution, and that the first three grids are not adequate to simulate the current case.

4.3.2. Validation and comparative study

In this section numerical results are compared with experimental data from Van Heiningen [4]. As mentioned previously, the same boundary conditions, as those applied by Heyerichs and Pollard [20] and Wang and Mujumdar [30], have been used. However, as was pointed out by Shi et al. [32] inlet conditions are critical in impinging plane jets evaluation. Thus, a study of the influence of turbulence level and different velocity profiles at the nozzle exit on Nusselt number is also carried out.

For the studied case, velocity and turbulent stresses are not reported in the experimental study; thus the analysis is restricted to the thermal field. The parameter compared is the Nusselt number at the impingement plate. The Nusselt number has been determined as: $Nu = \frac{[\partial T/\partial y]_w}{(T_w - T_{in})/B}$, where T_w is the impingement plate temperature and T_{in} the inlet jet temperature.

The calculated Nusselt number is presented together with experimental results in Fig. 16a for k–ϵ based models and in Fig. 16b for k–ω models.

4.3.2.1. Stagnation region. Models using ω like dissipation variable perform better than models using ϵ variable (see Fig. 16). The model that most correctly predicts local Nusselt at stagnation point is the WXT ($k\omega$-LEVM) model (see Fig. 16b), followed for the CLS ($k\epsilon$-NLEVM) model, which shows better behaviour than IL ($k\epsilon$-LEVM) model and similar to GPC ($k\epsilon$-LEVM) model in this region (see Fig. 16a). LAR ($k\omega$-NLEVM) model comes next. It predicts a local Nusselt at the stagnation point closer to experiments than WX ($k\omega$-LEVM) model, which is its linear counterpart (see Fig. 16b). The worst result is exhibited by AMGS ($k\epsilon$-EARSM) model, because it is a high-Reynolds model. The same trend has been observed by Abdon and Sundén [33] for LAR ($k\omega$-NLEVM) and AMGS ($k\epsilon$-EARSM) models.

In the stagnation region, the use of extra-terms in the length scale determining equation, such as YAP correction together with adequate damping functions, rather than the relation used to evaluate the turbulent stress tensor it seems to be more important [21,33]. For example, Fig. 17 shows CLS model prediction using linear, quadratic and the complete set of terms in the constitutive relation. It reveals that second and third order terms have a small influence in this region. Thus, it is shown that the results in the stagnation zone mostly depend on the coefficient (C_μ, C^*_μ) used in the linear term of the constitutive relation.

4.3.2.2. Secondary maximum. The secondary maximum is attributed to a transition phenomena [34] due to an important increment of turbulence [35,33], three-dimensional effects or impingement of secondary eddies [34].

In this work it has been found that the second Nu maximum coincides with a steep positive gradient in the turbulence level near the bottom wall for IL ($k\epsilon$-LEVM), CLS ($k\epsilon$-NLEVM) and WXT ($k\omega$-LEVM) models. It is also observed that GPC ($k\epsilon$-LEVM), WX ($k\omega$-LEVM), ARG

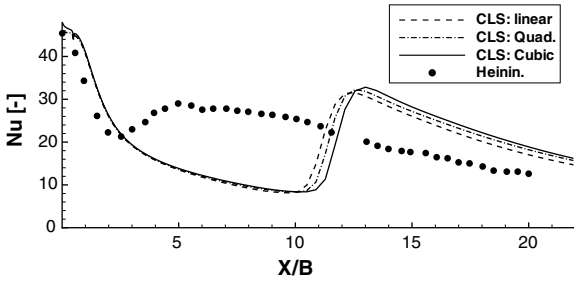

Fig. 17. Impinging jet. Nusselt number for different truncation levels of non-linear constitutive relation for CLS model. - - - linear terms; – · – · – including quadratic terms; —— complete model.

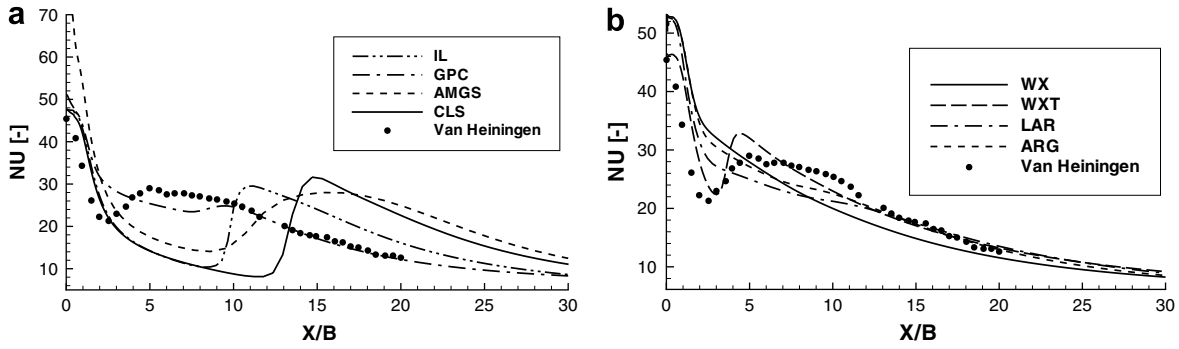

Fig. 16. Impinging jet. Validation: local Nusselt impingement plate. Lines numerical results and symbols experiments by Van Heiningen. [4]. (a) k–ϵ models and (b) k–ω models.

($k\omega$-EARSM) and LAR ($k\omega$-NLEVM) models do not exhibit an enhancement of turbulence. Consequently, they do not present a secondary peak in the local Nusselt profile.

CLS ($k\epsilon$-NLEVM) and AMGS ($k\epsilon$-EARSM) models predict with delay the secondary peak of *Nu*. Moreover, ARG ($k\omega$-EARSM) and LAR ($k\omega$-NLEVM) models do not predict it. So, there is no significant benefit in the use of higher order terms in the constitutive relation for the turbulent stresses in this zone.

Fig. 17 shows the influence of second and third order terms in the non-linear relation using CLS ($k\epsilon$-NLEVM) model. The main difference is observed in the step gradient of the curve. Furthermore, as it is pointed out by Wilcox [6], IL ($k\epsilon$-LEVM) and CLS ($k\epsilon$-NLEVM) models employ a damping function, that can prevent, or at least delay, transition. In fact, it is observed that the critical Reynolds for ϵ may be smaller than that for k for these models, which is opposed to the desired effect.

Finally, it is important to highlight that the CLS ($k\epsilon$-NLEVM) model has been applied by other authors [10,19] to round impinging jets, exhibiting better results that the observed in plane jets. This is probably due to three-dimensional effects, inclusion of some different parameters in C_μ and the use of an alternative formulation for YAP correction applied by Craft et al. [19]. AMGS ($k\epsilon$-EARSM) and LAR ($k\omega$-NLEVM) models have also been applied to round jets by Abdon and Sundén [33], and a similar behaviour to that observed in slot jets is shown.

4.3.3. Influence of inlet boundary conditions on Nusselt number

For all situations studied in this part the same impinging air jet configuration has been maintained at $Re_B = 10\,200$ and $H/B = 2.6$. All boundary conditions have also been preserved as in Fig. 14a, but inlet boundary condition is modified in order to analyse its effect on Nusselt number. Three models are selected to carry out this study: GPC ($k\epsilon$-LEVM), WXT ($k\omega$-LEVM) and CLS ($k\epsilon$-NLEVM).

4.3.3.1. Influence of inlet profiles. A previous simulation of a plane channel, long enough to obtain a fully developed flow, is made. The results of this preliminary calculation are used to investigate the effect of two different profiles at the jet discharge on the local *Nu* number. In the first study, local values of the fully developed region are interpolated to obtain the nozzle exit profiles. Whereas, in the second test a mean value of all variables in the same region is calculated. This constant value obtained is used in the current calculation for the impinging jet.

Although in both situations integral values of momentum and turbulence are maintained at the same level at the nozzle exit, it is clear from Fig. 18 that, when local value distributions are taked into account, they change local Nusselt number profile, specially increasing it near the stagnation region. It may be due to the concentration of the jet momentum to the symmetry axis.

4.3.3.2. Influence of length scale at the nozzle exit. Due to the difficulty in measuring the length scale in experiments, two studies of its effect on local Nusselt number are carried out. First, local values for variables (velocities, temperature and turbulent kinetic energy) are taken from the fully developed channel region (in the same way as the previous study), but different local values for the turbulent dissipation variable are calculated like a function of the local value of k_{in}, and a given length scale (l_e), $\epsilon_{\text{in}} = C_\mu k_{\text{in}}^{1.5}/l_e$ in k–ϵ models and $\omega_{\text{in}} = k_{\text{in}}^{0.5}/l_e$ in k–ω models. The following values of $l_e = 4.5 \times 10^{-3}B$, $l_e = 1.35 \times 10^{-2}B$ and $l_e = 4.05 \times 10^{-2}B$ are considered. Results from this study are presented in Fig. 19. It is shown that the local Nusselt increases proportionally to the length scale used to evaluate dissipation variable in the impinging region for the LEVM, and for values of $x/B \leqslant 10$ for the NLEVM tested.

Moreover, when a constant value for velocity and turbulent quantities is considered at the nozzle exit, i.e. $v_{\text{in}} = f(Re)$ and $k_{\text{in}} = f(v_{\text{in}},\ I = 0.04)$ (see Fig. 14a), the effect of varying the length scale on the local Nusselt number has been found to be the same as the previous one. As l_e increases, the Nusselt number increases appreciably near stagnation region and downstream for $x/B < 10$. Similar results are presented by Wang and Mujumdar [30].

4.3.3.3. Influence of turbulence intensity. If instead of varying the length scale, it is now maintained constant at

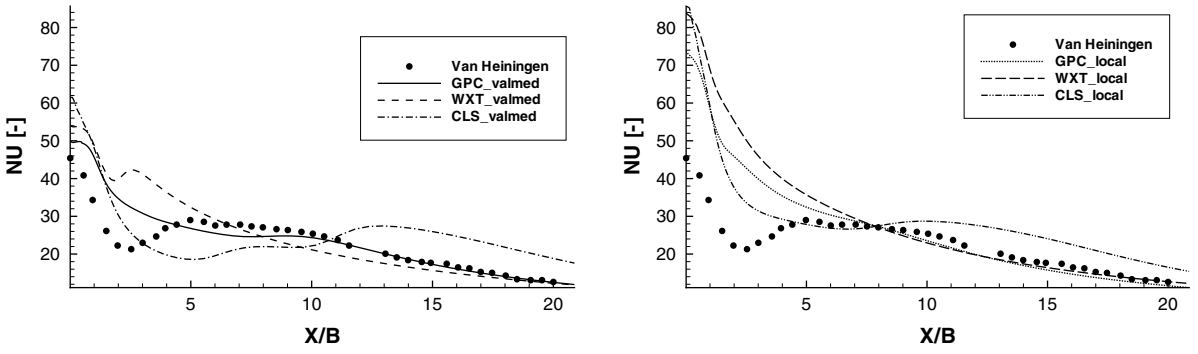

Fig. 18. Impinging jet. Comparison of the Nusselt number predicted by selected models when mean (constant) (left) and local (right) values from fully developed flow are imposed at the nozzle exit. Together with experimental data by Van Heiningen [4].

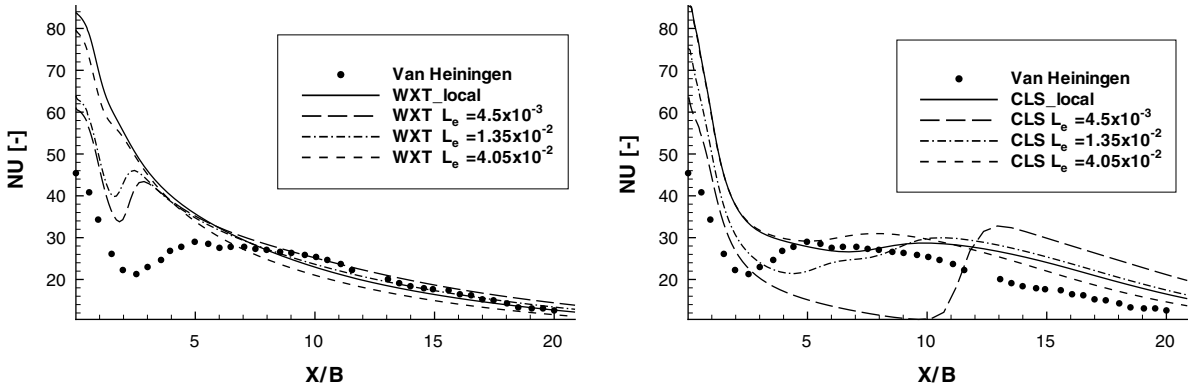

Fig. 19. Impinging jet. Effect of length scale on Nusselt number distribution with local values of variables in the inlet boundary condition. Left: WXT model, right: CLS model.

$l_e = 1.5 \times 10^{-2} B$, the turbulence intensity is changed from 0.01 to 0.08, and a mean value for inlet velocities is assumed, $v_{in} = f(Re)$, according to Fig. 14a. All models are sensitive to this parameter. The effect on the local Nusselt number distribution can be seen in Fig. 20. It is observed that NLEVM and LEVM using k–ϵ or k–ω platforms present a similar behaviour. Local Nusselt is increased near stagnation region and the secondary peak tends to disappear. However, some models are more sensitive to the inlet condition imposed, for example, CLS ($k\epsilon$-NLEVM) model presents a major variation near the stagnation region. The Nu number in this region (and downstream) is strongly influenced by the turbulence level near the bottom wall, and in this work is observed that an important factor in the turbulence level predicted in the stagnation zone is the y-direction turbulent normal stress.

Finally, it must be kept in mind that unlike the length scale, the turbulent intensity can be easily determined in experimental measurements.

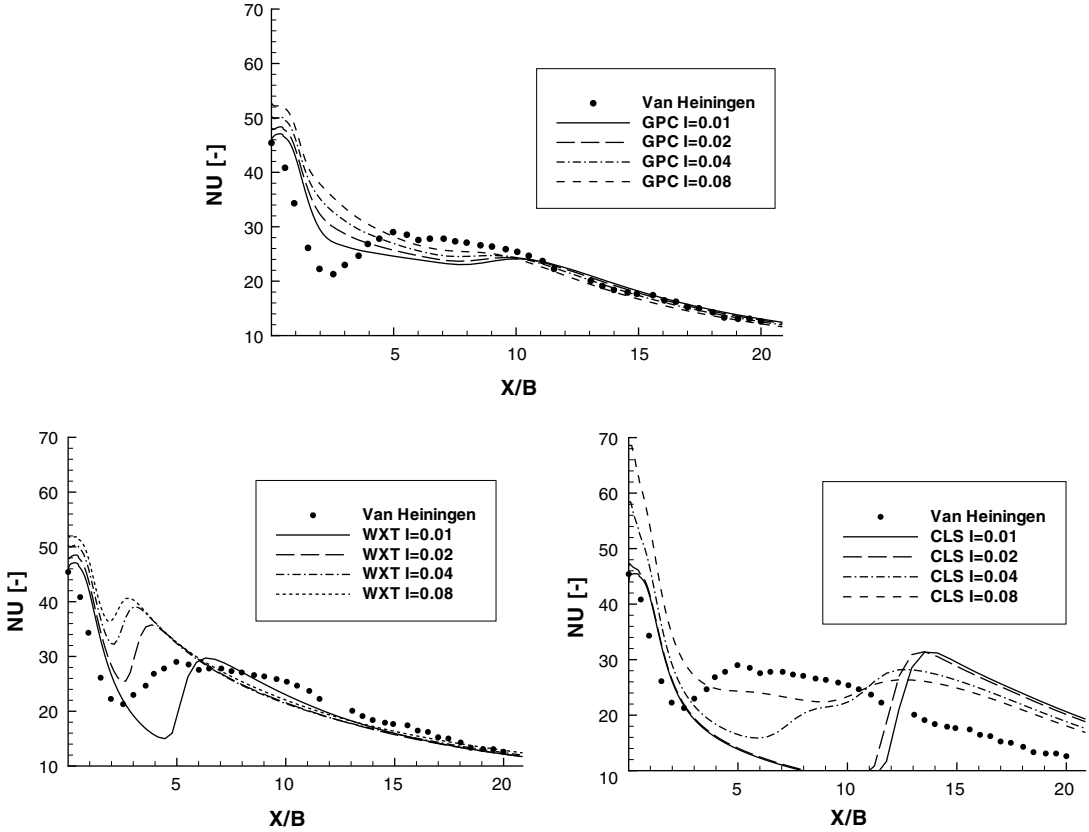

Fig. 20. Impinging jet. Effect of turbulence intensity on Nusselt number distribution, all variables are considered constant at the nozzle exit. Top: GPC model. Left: WXT model, right: CLS model.

5. Conclusions

Three basic test cases have been studied using linear and non-linear eddy viscosity models (LEVM, NLEVM) and explicit algebraic Reynolds stress models (EARSM), based on k–ϵ as well as k–ω platforms.

A verification procedure has been applied in order to ensure the credibility of numerical results. In general, reasonable values for the uncertainty and the order of accuracy of the numerical solution have been obtained. Some exceptions found were analysed in detail.

Reviewing the plane channel, which is the simplest case studied, non-linear or explicit algebraic models show reasonably good behaviour. These kind of models improve results of linear models, and they do not demand a major computational effort in this configuration.

In the case of backward facing step flow, NLEVM improve the accuracy in the predictions of skin friction coefficient and reattachment point, while the improvements in Stanton number, Reynolds stress tensor and mean velocity fields are limited. For these kind of flows, models such as CLS ($k\epsilon$-NLEVM) or ARG ($k\omega$-EARSM) should be used if a good prediction of global parameters, mean variables and qualitative turbulent stresses is desired.

Terms of higher order in the relation between turbulent stresses and mean strain rates do not improve considerably results in the impinging jet case for the models studied. Whereas the use of better tuned dumping functions and/or additional terms, such as YAP correction, in the length-scale determining equation seems to play a more important role. However, NLEVM slightly improve the predicted local Nusselt number compared with LEVM at the stagnation point.

When different turbulence intensities and velocity profiles are imposed at the inlet, all models studied exhibit different local Nusselt distribution until a critical value of X/B is achieved. Moreover, the effect of turbulence length scale at the nozzle exit produces significant changes in the Nusselt number distribution, but only near impinging region.

Throughout this work it has been found that the use of ω like length-scale quantity produces better results near solid walls. These models have presented better convergence and stability properties than k–ϵ models. Moreover, robustness of NLEVM and EARSM reduces when the complexity of the flow pattern increases (e.g. impinging jet) and the grid is densified.

Table 8
High Reynolds coefficients for k–ϵ models

Model	C_μ	$C_{\epsilon 1}$	$C_{\epsilon 2}$	σ_k	σ_ϵ
IL [7]	0.09	1.44	1.92	1.00	1.30
GPC [8]	0.09	1.44	1.92	1.00	1.30
CLS [19]	$\min\left[0.09, \frac{1.2}{1+3.5\eta+frs}\right]$	1.44	1.92	1.00	1.30
AMGS [12]	0.081	1.44	1.83	1.00	1.5544

Acknowledgement

The research has been financially supported by the 'Ministerio de Ciencia y Tecnología', Spain (Ref. TIC 2003-07970).

Appendix A

In Table 8 a summary of model closure coefficients is shown. Table 9 shows extra terms for damping functions in low Reynolds version summarised for k–ϵ models, where $\tau = \frac{k}{\epsilon}$.

In Tables 8 and 9:

- $\eta = \max[\overline{S}, \overline{W}]$, $\overline{S} = \sqrt{2\mathbf{SS}}$, $\overline{W} = \sqrt{2\mathbf{WW}}$.
- $y^+ = \frac{\rho x_n u_\tau}{\mu_t}$, $u_\tau = \sqrt{\tau_w/\rho}$ is friction velocity and x_n is the distance to the nearest wall.
- $\mathrm{YAP} = \max\left[0.83\rho\left(\frac{k^{3/2}}{2.5\tilde{\epsilon}x_n} - 1\right)^2 \frac{\tilde{\epsilon}^2}{k}, 0\right]$, $\mathrm{frs} = 0.235(\max(0, \eta - 3.333))^2 \exp^{-\frac{R_t}{400}}$.
- $R_t = \frac{k^2}{\nu\epsilon}$, $T_t = \frac{k}{\epsilon}\max[1, \sqrt{2/R_t}]$, $R_y = \frac{\sqrt{k}y}{\nu}$.
- $\vartheta = \max[k^{1/2}, (\nu\epsilon)^{1/4}]$, $\Psi = \max\left[\frac{\partial k}{\partial x_j}\frac{\partial (k/\epsilon)}{\partial x_j}, 0\right]$.

Table 10 shows the different parameters for k–ω models $\left(R_\omega = \frac{\rho k}{\omega\mu}\right)$.

Table 9
Viscous terms in low Reynolds k–ϵ models

Model	IL [7]	GPC [8]	CLS [10]	AMGS [12]
f_μ	$\exp\left(\frac{-3.4}{(1.0+R_t/50)^2}\right)$	$\frac{1-\exp[-0.01R_t]}{1-\exp[-\sqrt{R_t}]}\max[1, \sqrt{2/R_t}]$	$1-\exp\left[-\sqrt{R_t/90} - (R_t/400)^2\right]$	1.0
D	$2\mu\left(\frac{\partial\sqrt{k}}{\partial x_j}\right)^2$	0.0	$2\mu\left(\frac{\partial\sqrt{k}}{\partial x_j}\right)^2$	0.0
f_1	1.0	1.0	1.0	1.0
f_2	$1-0.3\exp[-R_t^2]$	1.0	$1-0.3\exp[-R_t^2]$	$1-\exp\left(-\frac{R_y}{12.5}\right)$
E	$2\nu\mu_t\left(\frac{\partial^2\bar{u}_i}{\partial x_j \partial x_k}\right)^2$	$\frac{0.3\rho\vartheta\sqrt{\epsilon T_t}\Psi}{T_t}$	$0.0022\frac{\overline{S}\mu_t k^2}{\rho\tilde{\epsilon}}\left(\frac{\partial^2\bar{u}_i}{\partial x_j \partial x_k}\right)^2$, $R_t < 250$	0.0
Y_c	YAP	0.0	YAP	0.0

Table 10
Model parameters for k–ω models

Model	WX [6]	WXT [9]	LAR [13]	ARG [14]
α^*	1.0	$\frac{1.0/40 + R_\omega/6.0}{1 + R_\omega/6.0}$	$\frac{1}{6.5 + \sqrt{6}\cos(0.333a\cos\sqrt{6}W^*)U^*T}$	1.0
β^*	0.09	$\frac{9.0(5.0/18 + (R_\omega/8.0)^4)}{100(1 + (R_\omega/8.0)^4)}$	0.09	1.0
α	5.0/9.0	$\frac{5.0(1.0/10 + R_\omega/2.7)}{9.0(1.0 + R_\omega/2.7)}(\alpha^*)^{-1}$	5.0/9.0	0.5467
β	3.0/40	3.0/40	3.0/40	0.83
σ_k	2.0	2.0	2.0	1.4
σ_ω	2.0	2.0	2.0	2.0

Table 11
Coefficients for non-linear stress–strain relationship

Model	AMGS [12]	CLS [10]	LAR [13]	ARG [14]
C^*_μ	$\alpha_1\frac{3(1+\eta^2)+0.2(\eta^6+\xi^6)}{3+\eta^2+6\eta^2\xi^2+6\xi^2+\eta^6+\xi^6}$	C_μ	C_μ	$\alpha_1\frac{3(1+\eta^2)}{3+\eta^2+6\eta^2\xi^2+6\xi^2}$
f^*_μ	1.0	f_μ	1.0	1.0
β_1	$\alpha_5 C^*_\mu$	$-0.4C^*_\mu f^*_\mu$	0.0	$\alpha_5 C^*_\mu$
β_2	$\alpha_4 C^*_\mu$	$0.4C^*_\mu f^*_\mu$	$2\frac{\sqrt{1-(3C_\mu S^*T)^2}}{1+6S^*\Omega^*T^2}$	$\alpha_4 C^*_\mu$
β_3	0.0	$-1.04C^*_\mu f^*_\mu$	0.0	0.0
γ_1	0.0	$40(C^*_\mu)^3 f^*_\mu$	0.0	0.0
γ_2	0.0	$40(C^*_\mu)^3 f^*_\mu$	0.0	0.0

At the solid walls non-slip boundary condition is used $\vec{v}_{\text{wall}} = 0$. At that point, turbulent kinetic energy disappears, $k_{\text{wall}} = 0$, and the value imposed for ϵ or ω depends on the model applied:

- k–ϵ models, $\epsilon_{\text{wall}} = 2\nu\left(\frac{\partial\sqrt{k}}{\partial x_n}\right)^2$ or $\tilde{\epsilon}_{\text{wall}} = 0$.
- k–ω models, $\omega_{\text{wall}} = \frac{6\nu}{\beta x_n^2}$.

Table 11 shows the coefficients used for NLEVM and EARSM in their relation in the Reynolds stress tensor. For C_μ and f_μ functions see Tables 8 and 9 respectively.

In Table 11 both models AMGS and ARG use:

- $\eta^2 = \alpha_2(S_{ij}S_{ij})(\tau^2),\ \xi^2 = \alpha_3(W_{ij}W_{ij})(\tau^2)$,
- $\alpha_1 = (4/3 - C_2)(g/2),\ \alpha_2 = (2 - C_3)^2(g^2/4)$, $\alpha_3 = (2 - C_4)^2(g^2/4)$,
- $\alpha_4 = \left(\frac{2-C_4}{2}\right)g,\ \alpha_5 = (2 - C_3)g,\ g = \frac{1}{0.5C_1+C_5-1}$, while AMGS model uses
- $C_1 = 6.8,\ C_2 = 0.36,\ C_3 = 1.25,\ C_4 = 0.40,\ C_5 = 1.88$ and $\tau = \frac{k}{\epsilon}$.

ARG model uses

- $C_1 = 3.0,\ C_2 = 0.8,\ C_3 = 1.75,\ C_4 = 1.31,\ C_5 = 2.0$ and $\tau = \frac{1}{\omega}$.

For LAR model

- $U^* = \sqrt{S_{ij}S_{ij} + W_{ij}W_{ij}},\ \Omega^* = \sqrt{W_{ij}W_{ij}},\ S^* = \sqrt{S_{ij}S_{ij}}$,
- $W^* = \frac{S_{ij}S_{jk}S_{ki}}{(S^*)^3},\ T = \tau = \frac{1}{\beta^*\omega}$.

References

[1] S. Pope, Turbulent Flows, Cambridge University Press, 2000.
[2] R. Moser, J. Kim, N. Mansour, Direct numerical simulation of turbulent channel flow up to $Re_\tau = 590$, Phys. Fluids 11 (1999) 943–945.
[3] D. Driver, H. Seegmiller, Features of a reattaching turbulent shear layer in divergent channel flow, AIAA J. 23 (1985) 163–171.
[4] A.V. Heiningen, Heat transfer under impinging slot jet, Ph.D. thesis, McGill University, 1982.
[5] J. Cadafalch, C. Pérez-Segarra, R. Còsul, A. Oliva, Verification of finite volume computations on steady state fluid flow and heat transfer, J. Fluids Eng. 124 (2002) 11–21.
[6] D. Wilcox, Turbulence modeling for CFD, DCW Industries, Inc., CA, 1998.
[7] N. Ince, B. Launder, Computation of buoyancy-driven turbulent flows in rectangular enclosures, Int. J. Heat Fluid Flow 10 (1) (1989) 110–117.
[8] U. Goldberg, O. Peroomian, S. Chakravarthy, A wall-distance-free k–ϵ model with enhanced near-wall treatment, J. Fluids Eng. 120 (1998) 457–462.
[9] D.C. Wilcox, Simulation of transition with a two-equation turbulence model, AIAA J. 32 (1994) 247–255.
[10] T. Craft, B. Launder, K. Suga, Development and application of cubic eddy-viscosity model of turbulence, Int. J. Heat Fluid Flow 17 (1) (1996) 108–115.
[11] T. Gatski, C. Speziale, On explicit algebraic stress models for complex turbulent flows, J. Fluid Mech. 254 (1) (1993) 59–78.
[12] R. Abid, J. Morrison, T. Gatski, C. Speziale, Prediction of aerodynamic flows with a new explicit algebraic stress model, AIAA J. 34 (12) (1996) 2632–2635.
[13] J. Larsson, Two-equation turbulence models for turbine blade heat transfer simulations, in: Proceedings 13th ISABE Conference, 1997, pp. 1214–1222.

[14] R. Abid, C. Rumsey, T. Gatski, Prediction of nonequilibrium turbulent flows with explicit algebraic stress models, AIAA J. 33 (11) (1995) 2026–2031.
[15] C. Pérez-Segarra, A. Oliva, M. Costa, F. Escanes, Numerical experiments in turbulent natural and mixed convection in internal flows, Int. J. Numer. Methods Heat Fluid Flow 5 (1) (1995) 13–33.
[16] S.V. Patankar, Numerical Heat Transfer and Fluid Flow, Hemisphere Publishing Corporation, 1980.
[17] M. Darwish, F. Moukalled, An efficient very-high resolution scheme based on an adaptive-scheme strategy, Numer. Heat Transfer, Part B 34 (1998) 191–213.
[18] B. Hutchinson, G.D. Raithby, A multigrid method based on the additive correction strategy, Numer. Heat Transfer, Part B 9 (5) (1986) 511–537.
[19] T. Craft, H. Iacovides, J. Yoon, Progress in the use of non-linear two-equation models in the computation of convective heat-transfer in impinging and separated flows, Flow Turbulence Combust. 63 (1) (1999) 59–81.
[20] K. Heyerichs, A. Pollard, Heat transfer in separated and impinging turbulent flows, Int. J. Heat Mass Transfer 39 (12) (1996) 2385–2400.
[21] D. Apsley, M. Leschziner, Advanced turbulence modelling of separated flow in a diffuser, Flow Turbulence Combust. 63 (1) (1999) 81–112.
[22] M. Ozisik, Heat Transfer. A Basic Approach, McGraw-Hill, 1985.
[23] J. Eaton, J.P. Johnston, A review of research on subsonic turbulent flow reattachment, AIAA J. 19 (1981) 1093–1100.
[24] J. Vogel, J. Eaton, Combined heat transfer and fluid dynamic measurements, J. Heat Transfer 107 (1985) 922–929.
[25] J. Kim, S.J. Kline, J.P. Johnston, Investigation of a reattaching turbulent shear layer: flow over a backward-facing step, J. Fluids Eng. 102 (1980) 302–308.
[26] T.S. Park, H. Sung, A Nonlinear low-Reynolds-number k–ϵ model for turbulent separated and reattaching flows – I. Flow field computations, Int. J. Heat Mass Transfer 38 (1995) 2657–2666.
[27] S. Thangam, C.G. Speziale, Turbulent flow past a backward-facing step: a critical evaluation of two-equation models, AIAA J. 30 (1992) 1314–1320.
[28] J. Jaramillo, K. Claramunt, C. Pérez-Segarra, R. Còsul, J. Cadafalch, Numerical study of different RANS models applied to turbulent forced convection, in: Proceedings of the IV International Symposium on Turbulence, Heat and Mass Transfer, 2003, pp. 671–680.
[29] R. Gardon, J.C. Akfirat, Heat transfer characteristics of impinging two-dimensional air jets, J. Heat Transfer 88 (1) (1966) 101–108.
[30] S. Wang, A. Mujumdar, A comparative study of five low Reynolds number k–ϵ models for impingement heat transfer, Flow Turbulence Combust. 25 (1) (2005) 31–44.
[31] S.H. Seyedin, M. Hasan, A.S. Mujumdar, Modelling of a single confined turbulent slot jet impinging using various k–ϵ turbulence models, Appl. Math. Modell. 18 (1994) 526–537.
[32] Y. Shi, M. Ray, A. Mujumdar, Computational study of impingement heat transfer under a turbulent slot jet, Ind. Eng. Chem. Res. 41 (2002) 4643–4651.
[33] A. Abdon, B. Sundén, Numerical investigation of impingement heat transfer using linear and non-linear two-equation turbulence models, Numer. Heat Transfer, Part A 40 (2001) 563–578.
[34] T.H. Park, H. Choi, J. Yoo, S. Kim, Streamline upwind numerical simulation of two-dimensional confined impinging slot jets, Int. J. Heat Mass Transfer 46 (2) (2003) 251–262.
[35] M. Behnia, S. Parneix, Y. Shabany, P. Durbin, Numerical study of turbulent heat transfer in confined and unconfined impinging jets, Int. J. Heat Fluid Flow 20 (1) (1999) 1–9.